

See discussions, stats, and author profiles for this publication at: <https://www.researchgate.net/publication/263990760>

Thermal Conductivity of High-Modulus Polymer Fibers

ARTICLE *in* MACROMOLECULES · JUNE 2013

Impact Factor: 5.8 · DOI: 10.1021/ma400612y

CITATIONS

24

READS

103

4 AUTHORS, INCLUDING:



[Xiaojia Wang](#)

University of Minnesota Twin Cities

17 PUBLICATIONS 227 CITATIONS

SEE PROFILE



[David G Cahill](#)

University of Illinois, Urbana-Champaign

364 PUBLICATIONS 13,933 CITATIONS

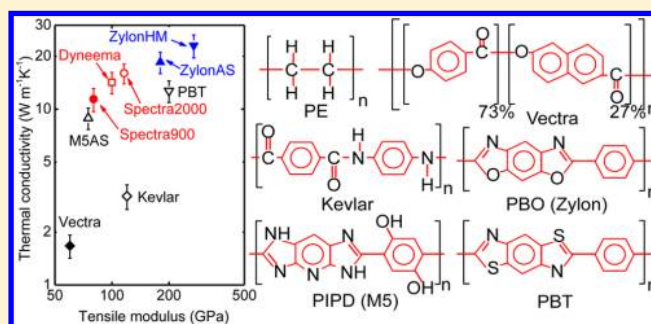
SEE PROFILE

Thermal Conductivity of High-Modulus Polymer Fibers

Xiaojia Wang,^{*,†} Victor Ho,[‡] Rachel A. Segalman,[‡] and David G. Cahill^{*,†}[†]Department of Materials Science and Engineering, and Materials Research Laboratory, University of Illinois, Urbana, Illinois 61801, United States[‡]Department of Chemical and Biomolecular Engineering, University of California, Berkeley, Berkeley, California 94720, United States

S Supporting Information

ABSTRACT: Polymers have many desirable properties for engineering systems—e.g., low mass density, chemical stability, and high strength-to-mass ratio—but applications of polymers in situations where heat transfer is critical are often limited by low thermal conductivity. Here, we leverage the enormous research and development efforts that have been invested in the production of high-modulus polymer fibers to advance understanding of the mechanisms for thermal transport in this class of materials. Time-domain thermoreflectance (TDTR) enables direct measurements of the axial thermal conductivity of a single polymer fiber over a wide temperature range, $80 < T < 600$ K. Relaxation of thermoelastic stress in the Al film transducer has to be taken into account in the analysis of the TDTR data when the laser spot size is small because the radial modulus of the fiber is small. This stress relaxation is controlled by the velocity of the zero-order symmetric Lamb mode of a thin Al plate. We find similarly high thermal conductivities of $\Lambda \approx 20 \text{ W m}^{-1} \text{ K}^{-1}$ in crystalline polyethylene and liquid crystalline poly(*p*-phenylene benzobisoxazole). For both fiber types, $\Lambda(T) \propto 1/T$ near room temperature, suggesting an intrinsic limit to the thermal conductivity governed by anharmonicity, not structural disorder. Because of the high degree of elastic anisotropy, longitudinal acoustic phonons with group velocities directed along fiber axis are likely to be the dominate carriers of heat.



1. INTRODUCTION

Polymeric materials typically have a low thermal conductivity of $\Lambda \approx 0.2 \text{ W m}^{-1} \text{ K}^{-1}$ near room temperature,¹ and, in fact, foams of amorphous polymers are widely used for thermal insulation. Materials for heat exchangers and thermal management, however, require high Λ that is commonly provided by nearly pure metals (Cu, Al, Ti) and ceramics (AlN, diamond, graphite). Recent reports of extraordinarily high Λ in polyethylene nanofibers and natural biopolymers have renewed interest in thermally conductive polymers.^{2,3}

More than 30 years ago, Choy and co-workers demonstrated that alignment of polymer crystallites can significantly enhance both the mechanical strength and thermal conductivity Λ of polymers along the direction of the covalently bonded molecular chains.^{4–9} We can therefore expect that molecular alignment produced by gel-spinning, drawing, or extrusion used in the production of high-performance fibers could result in significant enhancement of Λ . However, most previous work has focused on extruded polymer films or sheets.^{5,7,10} Studies of the thermal conductivity of polymer fibers are relatively limited and mostly confined to polyethylene (PE) and polybenzobisoxazole (PBO).^{2,11,12}

Choy et al. studied the temperature dependence of the thermal conductivity $\Lambda(T)$ of fiber-reinforced plastics (FRP) consisting of Spectra 1000 and low-density PE with varying fiber volume fractions.¹¹ They reported an axial thermal conductivity of $\Lambda \approx 30 \text{ W m}^{-1} \text{ K}^{-1}$ at 300 K for the FRP

with the largest filling ratio of 0.73.¹¹ Fujishiro and colleagues measured Λ of Dyneema and Zylon fibers at temperatures from 15 to 260 K. They studied both fiber bundles and FRPs and reported $\Lambda \approx 60 \text{ W m}^{-1} \text{ K}^{-1}$ at 260 K for both Dyneema and Zylon.¹² Both groups used conventional steady-state measurement techniques that are prone to errors created by radiative heat transfer, particularly for samples with high aspect ratios. For example, the length-to-width aspect ratios of the specimens investigated in ref 12 were approximately 50:1.

Recently, $\Lambda \approx 100 \text{ W m}^{-1} \text{ K}^{-1}$ was reported² by Shen et al. for a single polyethylene nanofiber measured using a bimaterial microcantilever as a heat flux sensor. The nanofiber was formed by attaching the nanofiber to either a tungsten tip or an AFM cantilever and pulling at elevated temperatures to achieve a diameter of $\approx 130 \text{ nm}$ and a length of $\approx 290 \mu\text{m}$. Because of experimental limitations, the measurement approach could not be applied to micro-sized fibers or otherwise validated with reference samples with known properties.

In the present work, we apply time-domain thermoreflectance (TDTR), an ultrafast pump–probe laser technique, to measure Λ of nine high-modulus polymer fibers along the fiber direction at room temperature. TDTR has sufficient spatial resolution to measure an individual $\approx 10 \mu\text{m}$ diameter fiber.

Received: March 25, 2013

Revised: May 25, 2013

Published: June 5, 2013

TDTR has been thoroughly validated on a wide variety of materials that span a wide range of Λ .¹³ The thermal conductivities of two types of polyethylene fibers (Dyneema and Spectra 900) and one liquid crystal polymers (Zylon AS) are also measured as functions of the temperature to provide insights on the mechanisms and limits of heat transport in these materials.

2. EXPERIMENTAL INVESTIGATION

2.1. Sample Fabrication and Characterization. The nine polymer fibers we studied include both crystalline polymers and liquid crystal polymers (LCP). The crystalline polymer fibers are Dyneema SK75 (ultrahigh molecular weight polyethylene with a crystallinity of $\approx 80\%$) from DSM Dyneema LLC and Spectra 900/2000 (high-density polyethylene) from Honeywell. LCP fibers with rod-like segments include Vectra, Kevlar, poly(*p*-phenylene benzobisoxazole) (PBO), polyhydroquinone diimidazopyridine (PIPD), and poly(*p*-phenylene benzobisthiazole) (PBT). Vectra fibers were obtained from Celanese. Kevlar 149 fibers were obtained from E.I. du Pont De Nemours and Company. Both Zylon as-spun (Zylon AS, PBO) and Zylon high-modulus (Zylon HM, PBO) fibers were provided by Toyobo Co., Ltd. The M5 as-spun (M5 AS, PIPD) fibers, originally developed by Akzo Nobel, were supplied by the U.S. Army Natick Research, Development and Engineering Center. The PBT fibers were obtained from two producers: E.I. du Pont De Nemours and Company and Celanese. The diameters of the fibers range from 10 to 30 μm .

Figure 1 summarizes the chemical structures of the fibers. The LCP fibers span a wide range of interchain bonding strengths. PBO (Zylon)

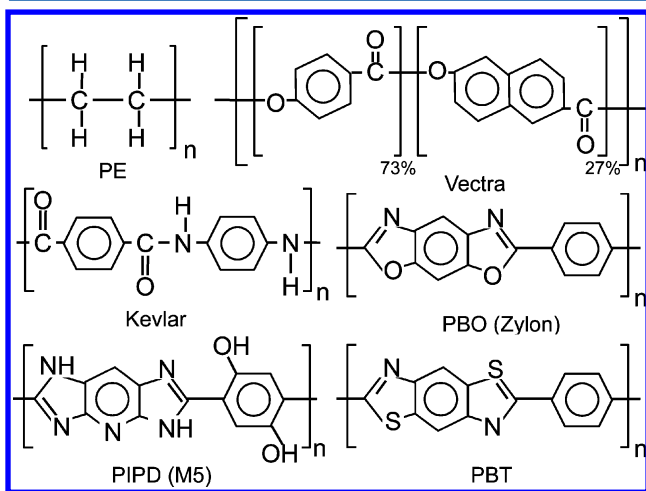


Figure 1. Molecular structures of nine polymer fibers with high tensile moduli.

has relatively weak interchain bonding. Vectra, Kevlar, and PIPD (M5 AS) have progressively stronger interchain bonding due to increasing densities of lateral hydrogen bonds. The bidirectional hydrogen bonds of M5 AS result in a 3D network structure that is thought to enhance the compressive modulus.¹⁴

Sample preparation consists of three main steps: (i) embedding fibers in an epoxy matrix, (ii) microtoming with a diamond blade, and (iii) deposition of the Al metal film transducer. The embedding material is cross-linked epoxy prepared by blending two mixtures before use: mixture A of a resin (LX112, Ladd Research Industries, Inc.) and a plasticizer (DDSA, Ted Pella, Inc.) in the mass ratio of 1:1.25 and mixture B of the same resin and a hardener (NMA, Ted Pella, Inc.) in the mass ratio of 7:6.3. DMP-30 (Polysciences, Inc.) in the proportion of 1.5% was added to accelerate the cure rate. The mixture was degassed for ≈ 40 min under vacuum at ≈ 35 °C before transferring to the mold. We designed a mold that clamps the two ends of the fibers to keep the fibers well-aligned in the epoxy mixture.

The mixture was cured at 70 °C to form hard epoxy blocks. Microtoming was done with a Leica EM UC6 microtome. A 35° diamond knife (DIATOME) was used to produce fiber cross sections by cutting the epoxy blocks perpendicular to the fiber direction. Finally, a thin Al layer was deposited onto the sample surface in a magnetron sputter deposition system with a base pressure below 10^{-7} Torr. Al is commonly used as the transducer layer for TDTR because Al has a relatively high thermal conductivity, high thermorefectance, large piezo-optical coefficients, and good adhesion to most materials. The Al thickness can be determined by picosecond acoustics.¹⁵

TDTR measurements of thermal conductivity require samples with relatively smooth surfaces. Figure 2 shows representative atomic force

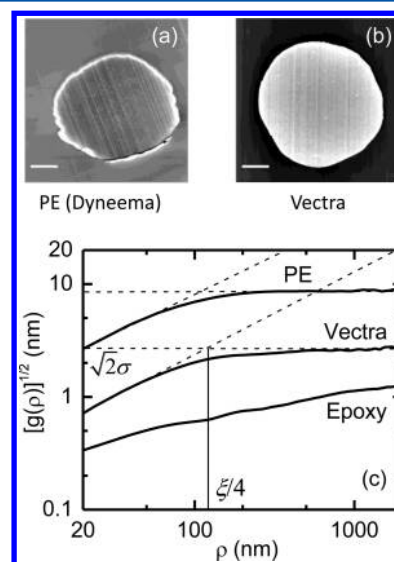


Figure 2. AFM images of microtomed surfaces: (a) Dyneema; (b) Vectra. The diameter of the fibers is ≈ 20 nm; the scale bars are 5 μm . The height variation from black-to-white is 160 nm for (a) and 40 nm for (b). (c) Square root of the height-difference correlation functions for microtomed surfaces of Dyneema, Vectra, and the epoxy matrix. Dashed lines show extrapolations of the behavior at small and large length scales used to determine the correlation length of the morphology.

microscopy (AFM) images of the microtomed surfaces of Dyneema and Vectra fibers. The fiber cross sections are flat and relatively smooth, with only some scoring in the direction of cutting caused by microscopic flaws in the edge of the diamond knife.

We quantify the surface morphology using the height-difference correlation function $g(\rho)$, which provides more extensive information about the surface features than the rms roughness (σ).^{16,17}

$$g(\rho) = \langle (h_i - h_j)^2 \rangle \quad (1)$$

where h_i and h_j are the heights at the surface positions i and j , respectively; ρ is the distance between surface points i and j ; and the brackets denotes an average over pairs of points i and j . We compare this measure of the surface morphology of microtomed surfaces of Dyneema, Vectra, and epoxy in Figure 2c. For separation distance ρ smaller than the in-plane correlation length ξ , $[g(\rho)]^{1/2}$ increases linearly with ρ , whereas for $\rho > \xi$, $[g(\rho)]^{1/2}$ saturates at $\sqrt{2}$ times the rms surface roughness. The in-plane correlation length scale ξ can be determined by the point of intersection ρ_c of fits to both the linear and saturated regimes $\xi = 4\rho_c$. We find $\xi \approx 450$ nm for both fibers. The microtomed surfaces of the fibers are sufficiently smooth for TDTR measurement with $[g(\rho)]^{1/2}$ less than 10 nm. We do not yet understand why the morphology of the microtomed fibers is significantly rougher than the microtomed epoxy.

2.2. Time-Domain Thermorefectance. We used time-domain thermorefectance (TDTR) to measure the thermal conductivity along

the axial direction of the fiber. In the TDTR approach, a mode-locked Ti:sapphire laser produces a train of pulses at a repetition rate of 80 MHz. The laser output is split into a pump beam and a probe beam with a relative optical path adjusted via a mechanical delay stage. The pump beam is modulated at a frequency of ≈ 10 MHz with an electro-optical modulator, and the probe beam is mechanically chopped at ≈ 200 Hz. The pump and probe beams are focused on the sample surface through a single objective lens. Diffusely scattered pump light is suppressed using orthogonal polarizations of the pump and probe, spectral and spatial separation of the pump and probe, and double modulation.¹⁸

We used a 20 \times objective lens with a $1/e^2$ radius of ≈ 2.7 μm for all fibers measured at room temperature. For some of the fibers with an average diameter of ≥ 20 μm , we also used a 10 \times objective lens with a $1/e^2$ radius of ≈ 5 μm . The fraction of the laser energy deposited on the surrounding epoxy is $\sim 1\%$ for a 10 μm fiber with the 20 \times objective lens and $< 0.1\%$ for a 20 μm fiber with the 10 \times objective lens. Since the signal in a TDTR measurement is generated by the product of the pump and probe energies, the portion of the TDTR signal that is generated by the surrounding epoxy is negligible.

Because of the small laser spot size used in the TDTR measurement, steady-state heating (ΔT_{ss}) of the probed region of the fiber may be an important issue. The laser power was optimized as a compromise between the signal-to-noise ratio and ΔT_{ss} . Unless otherwise noted, we used a laser spot size $w_0 = 2.7$ μm ; a total laser power of 6 mW then produces $\Delta T_{\text{ss}} \approx 10$ K at room temperature for fibers at the upper end of the range of thermal conductivities. For lower thermal conductivity fibers such as Vectra and Kevlar, we used a total laser power of 2 mW to maintain $\Delta T_{\text{ss}} < 10$ K. Detailed discussion on the estimation of ΔT_{ss} is provided in the Supporting Information.

For measurements at elevated temperatures, the sample was mounted on a ceramic heater with silver paint. The temperature was monitored by a Pt resistance thermometer mounted with the thermometer attached to the ceramic heater using silver paint. We used a He flow cryostat for low temperature measurements.

2.3. Wide-Angle X-ray Scattering. Wide-angle X-ray scattering (WAXS) at beamline 7.3.3 of the Advanced Light Source was used to characterize the degree of the crystalline alignment. The X-ray wavelength was 1.24 \AA with a focused spot size of ≈ 0.5 mm. The beamline was equipped with a Pilatus 1 M 2D hybrid pixel detector with a 168.7 mm \times 179.4 mm detector area. The detector possesses a vertical area between modules 8 pixel wide that does not detect signal. Fibers were oriented approximately in the horizontal plane of the detector and were slightly tilted in the fiber orientation to avoid the dead area. The Nika 2D data reduction package¹⁹ was used to convert the 2D diffraction pattern to intensity at a particular scattering vector, labeled on the left of the 2D diffraction patterns for fibers with known unit-cell crystal structures (see Supporting Information), as a function of the azimuthal angle. Since diffraction peaks at these scattering angles probed with this particular experimental configuration are dominated by crystalline diffraction, the measurement results are reliable for analyzing the crystallite alignment only. Background scattering due to air and intermolecular correlations not attributable to crystalline diffraction were subtracted by fitting excess scattered intensity with an exponential decay. Gaussian peak fitting in Igor Pro was used to determine the standard deviation of the peak width as a function of the azimuthal angle.

3. DATA ANALYSIS AND THERMAL MODELING

The in-phase signal (V_{in}) of TDTR measurements is approximately proportional to the time evolution of the temperature excursion of the Al film and, at short time delays, also contains information about the Al layer thickness from picosecond acoustics. The out-of-phase signal (V_{out}) is approximately proportional to the imaginary part of the temperature oscillations at the modulation frequency. We analyze the ratio of $-V_{\text{in}}/V_{\text{out}}$ to improve the sensitivity by

utilizing the information in the out-of-phase signal and to minimize artifacts created by variations of laser spot size and beam overlap as a function of delay time.²⁰ The thermal model contains several parameters: the thickness, volumetric heat capacity, thermal conductivity of the Al layer (h_{Al} , C_{Al} , Λ_{Al}) and the fiber (h , C , Λ), the thermal conductance of the Al/fiber interface (G), the beam spot size w_0 , and the anisotropy $\eta = \Lambda_{\perp}/\Lambda$. The model is only weakly dependent on the thermal conductivity perpendicular to the fiber axis, and we set $\Lambda_{\perp} = 0.2$ $\text{W m}^{-1} \text{K}^{-1}$, a typical value for disordered polymers.²¹ We treat Λ and G as adjustable parameters in the model. Further details can be found in refs 18 and 22. The penetration depth of heat into the fiber at the modulation frequency f , $\delta = (\Lambda/(\pi f c))^{1/2}$, is at most $\delta \approx 1$ μm . Therefore, the sample thickness and fiber diameter are not parameters in the model.

In semiconductor alloys²³ and a particular form of a-Si,²⁴ we, and others,^{25,26} have found the thermal conductivity measured by TDTR to depend on the choice of the modulation frequency. We searched for this effect in selected fibers and have not observed a significant frequency dependence.

Figure 3a shows the picosecond acoustic signals from a Dyneema fiber. The Al thickness is 58 ± 3 nm based on the Al speed of sound and the time delay at which the first downward acoustic echo appears.^{15,27} The acoustic reflection coefficient of the Al/fiber interface is $R = (Z_{\text{fiber}} - Z_{\text{Al}})/(Z_{\text{fiber}} + Z_{\text{Al}})$ where the acoustic impedances are Z_{Al} and Z_{fiber} , with $Z = \rho v$ being the product of the density and longitudinal speed of sound in each

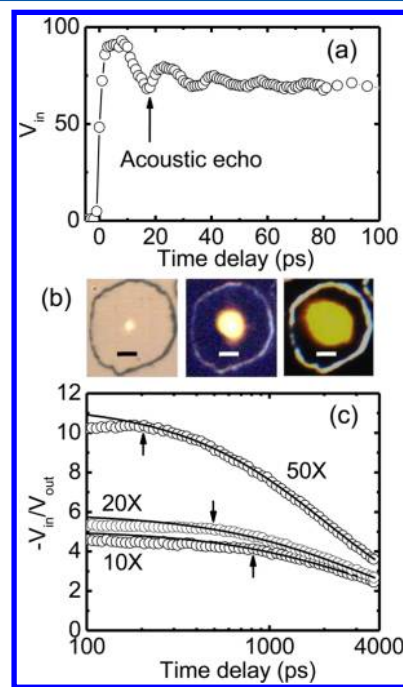


Figure 3. TDTR measurement of Dyneema fibers: (a) Short-time behavior of the V_{in} signal, measured with the 20 \times objective lens, used to determine the Al film thickness from the picosecond acoustic signals. (b) Optical microscopy images of the Dyneema fiber and the pump laser beam using, from left to right, 50 \times , 20 \times , and 10 \times objective lenses. The scale bars are 5 μm . (c) Long-time behavior of the ratio $-V_{\text{in}}/V_{\text{out}}$ used to determine the thermal conductivity measured with different objective lenses. The arrows mark the time delay at which the thermoelastic strain in the Al layer has fully decayed. The time scales, approximately the beam spot radius divided by the velocity of the zero-order symmetric Lamb mode of the Al transducer, are 200, 500, and 950 ps for the 50 \times , 20 \times , and 10 \times objective lenses, respectively.

medium. The downward shape of the first acoustic echo corresponds to a π phase shift of the strain wave at the Al/fiber interface indicating the acoustic impedance of the microtomed fiber is smaller than that of the Al transducer.

In Figure 3c, we plot the ratio $-V_{\text{in}}/V_{\text{out}}$ acquired using a series of objective lenses as a function of delay time. A noticeable feature in all of the data sets is the suppression of the ratio signal at short delay times; the locations where this suppression decays are marked by the arrows. We have not observed this feature previously in TDTR measurements for semiconductors, oxides, and metals. The mechanism that produces this feature in the signals is not yet clear, but we hypothesize that this feature is caused by a thermoelastic effect combined with the change in the Al reflectivity with strain. If the fiber sample beneath the metal transducer has small elastic constants for deformations perpendicular to the fiber axis, the lateral stress in the Al film generated by the pump beam can be relaxed by the propagation of an acoustic wave that is related to the zero-order symmetric Lamb mode of the thin Al film. As can be seen from Figure 3b, the stress relaxation occurs at ≈ 200 , 500, and 800 ps for beam spot sizes of 1.08, 2.7, and 5.2 μm , respectively, implying a propagation velocity on the order of 5.4 nm ps $^{-1}$. The velocity of the zero-order symmetric Lamb mode is $\nu_L = \xi\nu_s$, where ν_s and ξ are the shear velocity and the normalized phase velocity, respectively. Using $\xi = 1.73$ and $\nu_s = 3.15$ nm ps $^{-1}$ for a thin Al plate with Poisson's ratio of 0.33,²⁸ $\nu_L = 5.44$ nm ps $^{-1}$, in good agreement with the propagation velocity observed from TDTR measurements. In fitting the thermal model to the data, we exclude the region of delay time that is affected by this thermoelastic effect. Setting the two free-parameters to $\Lambda = 14$ W m $^{-1}$ K $^{-1}$ and $G = 52$ MW m $^{-2}$ K $^{-1}$ provides a good fit to the data acquired with all three laser spot sizes, as can be seen from Figure 3c.

The uncertainty of the TDTR measurement can be obtained by taking into account the individual uncertainties and sensitivities of the parameters in the thermal model.²⁹ At room temperature, the total uncertainty, combining both the standard deviations of measured individual fibers of the same type and the systematic errors, ranges from 13% to 16%. The uncertainty is expected to be slightly higher for low-temperature measurements due to the additional uncertainty from the steady-state and per-pulse heating as well as the deviations of in-plane thermal conductivity of the Al layer from the Wiedemann–Franz law (WFL). We use an average of $\sim 15\%$ as a simplified but reasonable estimation for the overall uncertainty at each temperature. Further details on the uncertainty analysis are described in the Supporting Information.

4. RESULTS AND DISCUSSION

4.1. Room Temperature Thermal Conductivity. The thermal conductivities Λ at room temperature are summarized in Figure 4. We use the reported axial modulus of each fiber as the x -axis of this plot to organize the data. The tensile moduli are taken from the company datasheets,^{30–34} previous literature,¹⁴ or polymer databases.³⁵ Previous studies have reported that the axial Λ of extruded or drawn polyethylene increases almost linearly with the axial tensile modulus.^{5,10,11,36} We are not proposing, however, that Λ is only controlled by the modulus or that the relationship between axial modulus and axial Λ is direct. The thermal conductivities of the PBT fibers from two sources (du Pont and Celanese) are close; the average value is plotted in Figure 4. We observe the highest Λ in PBO

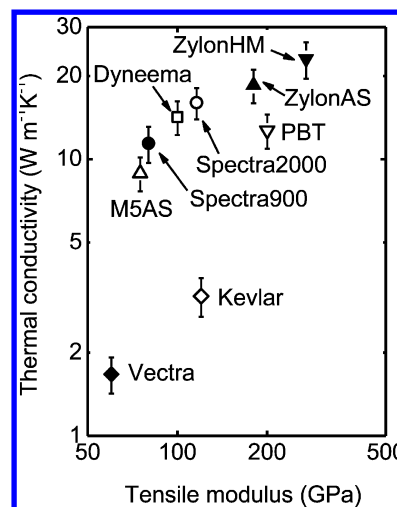


Figure 4. Thermal conductivities of various polymer fibers, measured with the 20 \times objective lens, as functions of their tensile moduli taken from the data sheets from the manufacturers. For each fiber type, the thermal conductivity is averaged over a minimum of four fibers. The error bars include both systematic errors and standard deviations of Λ measured for several fibers of the same type.

(19 W m $^{-1}$ K $^{-1}$ for Zylon AS and 23 W m $^{-1}$ K $^{-1}$ for Zylon HM).

In general, polymers with higher crystallinity and better chain alignment tend to have larger thermal conductivities.^{1,2,6} The low thermal conductivity of Vectra is probably attributable to the disorder in the chain segments; the relatively low crystallinity of $\sim 20\%$ as reported in ref 37 may also contribute to the low thermal conductivity. For LCP fibers with various chemical structures as depicted in Figure 1, the increase in the number of side chains in each molecular unit is likely to reduce the axial conductivity due to additional phonon scattering created by the vibrational modes of the side chains. We did not observe any dependence of the measured thermal conductivity on the dimensions of these microfibers.

4.2. Crystallite Orientation Degree. 2D resolved WAXS patterns are consistent with highly aligned crystallites within the polymer fibers as illustrated by well-defined and highly localized diffraction peaks perpendicular to the fiber axis. Data for representative fibers of Dyneema and Zylon HM are shown in Figure 5; the Supporting Information includes WAXS results of all fibers. We list the scattering angle and indices of peaks based on the measurement conditions and unit-cell structures of polyethylene (orthorhombic) and PBO (monoclinic) in Figure 5.^{38,39} We analyze the width of the Bragg diffraction peak (2θ) with 2-fold symmetry as a function of the azimuthal angle to characterize the degree of molecular orientation along the fiber direction. A smaller peak width corresponds to higher degrees of crystallite orientation. As can be seen from Table 1, the peak widths for all fibers are below 10 $^\circ$, and with the exception of Zylon AS and M5 AS, all are less than 6 $^\circ$.

We do not observe a clear dependence of the thermal conductivity Λ on the peak width. In particular, the materials with the highest Λ (Zylon AS and Zylon HM) have only relatively modest crystalline alignment. It is likely that due to the high absolute degree of alignment and small variation in peak widths in the samples, orientational contributions to the thermal conductivity are not as important as the differences in chemical structure of the polymer backbone and interchain bonding.

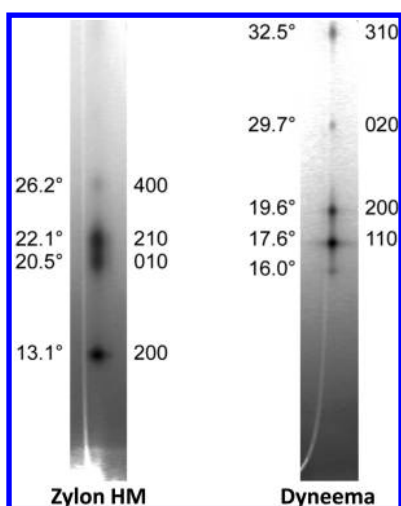


Figure 5. Representative 2D diffraction pattern for polymer fibers (Zylon HM and Dyneema). Diffraction peaks along the vertical are due to symmetry in the dimensions orthogonal to the chain axis (in the horizontal plane). Bragg 2θ conditions are presented on the left of the image and the corresponding index on the right. The unindexed reflection in Dyneema is commonly observed in polyethylene and has been attributed to the presence of a small fraction of the monoclinic polymorph.³⁸ It should be noted that the Bragg angles do not match in the images because two different sample–detector distances were used for experimental configurations. Intensities are presented on a log scale with magnitudes from white to black representing at least 2 orders of magnitude difference. The white spikes in both plots are caused by the gap between two detector modules.

Table 1. Polymer Fiber Peak Widths

sample	analyzed reflection ^a (deg)	peak width ^b (deg)
Spectra 900	17.6 (110)	2.3 ± 0.05
Spectra 2000	17.6 (110)	2.5 ± 0.05
Dyneema	17.6 (110)	2.8 ± 0.03
Vectra	16.8	4.6 ± 0.3
PBT	21.9 (010)	4.7 ± 0.1
Kevlar	17.6 (110)	5.3 ± 0.1
Zylon HM	20.5 (010)	5.6 ± 0.1
Zylon AS	20.5 (010)	6.1 ± 0.1
MS AS	23.4	9.4 ± 0.2

^aAnalyzed Bragg diffraction peak (2θ). Reflections with 2-fold symmetry with similar scattering vectors were selected to minimize differences in broadening caused by curvature of the Ewald sphere. Miller indices are given in parentheses for known indexed crystallographic reflections.^{38–40} ^bUncertainties reflect 95% confidence intervals in peak fits.

4.3. Temperature Dependence of the Thermal Conductivity. We measured the axial thermal conductivity as a function of temperature $\Lambda(T)$ for Zylon AS and two PE fibers (Dyneema and Spectra 900). The temperature of the data points has been corrected for the steady-state heating ΔT_{ss} discussed above as well as for the per pulse heating created by the pump optical pulses. This correction takes into account the temperature-dependent heat capacities for PE and PBO and the temperature-dependent thermal properties of the Al transducer. The final sample $\Lambda(T)$ at each temperature is found self-consistently.

In Figure 6, we compare our measurements of $\Lambda(T)$ of Zylon AS to prior data by Fujishiro and co-workers.¹² We believe that the data reported in ref 12 is strongly affected by radiation

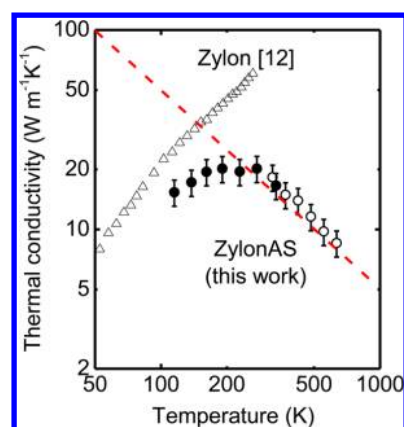


Figure 6. Temperature dependence of the thermal conductivity of Zylon AS fibers measured with the 20× objective lens. Filled circles are measured with samples mounted in a cryostat, and the open circles are measurements with a heating stage. The low-temperature data points are the average of values measured during cooling and heating. Previously published data in ref 12 for a Zylon bundle are reproduced for comparison. The dashed line in red indicates $1/T$ temperature dependence.

errors at $T > 200$ K. Our TDTR data for $\Lambda(T)$ increases with temperature from 100 to 200 K, has a broad maximum at ≈ 230 K, and decreases approximately as $1/T$ at $T > 300$ K.

In Figure 7, we compare our data for $\Lambda(T)$ of two PE fibers (Dyneema and Spectra 900) to prior studies of three types of PE: a composite of Spectra 1000 and low-density PE with a fiber volumetric ratio of 0.73,¹¹ a bundle of Dyneema fibers,¹²

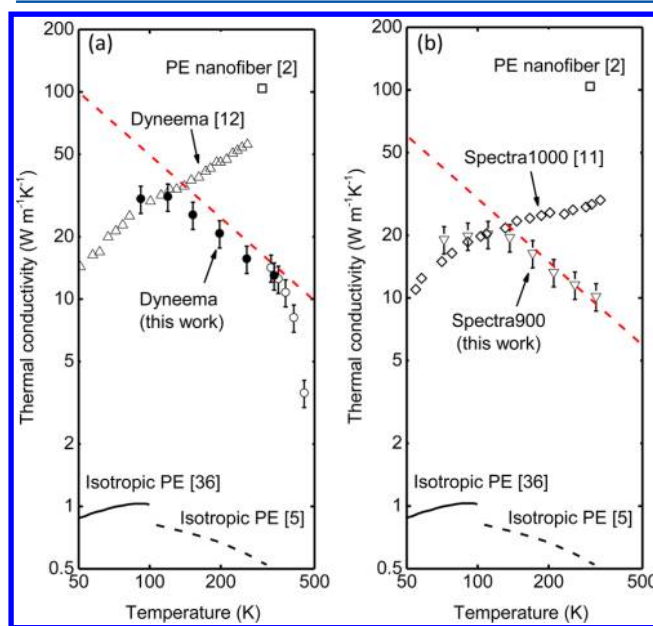


Figure 7. Temperature dependence of the thermal conductivity measured with the 10× objective lens (a) Dyneema and (b) Spectra 900. For Dyneema, filled circles are measured with samples mounted in a cryostat and the open circles are measurements with a heating stage. Prior work is included for comparison: a PE nanofiber from ref 2 (open square), a Dyneema bundle from ref 12 (upward open triangles), a composite of Spectra1000 and low-density PE with a fiber volumetric ratio of 0.73 from ref 11 (hollow open diamonds), and isotropic bulk PE from refs 5 and 36 (dashed and solid lines). The uncertainty is $\approx 15\%$. The dashed line in red indicates a $1/T$ temperature dependence.

and bulk samples of isotropic PE.^{5,36} Dyneema has a higher thermal conductivity than Spectra 900, but the trends of $\Lambda(T)$ for both fibers are similar and also resemble $\Lambda(T)$ for Zylon AS. The TDTR data suggest a broad maximum in $\Lambda(T)$ centered at ~ 100 K. The high-temperature measurement was limited by the melting temperature of PE of ≈ 415 K; therefore, the data point taken at ≈ 435 K for Dyneema is significantly lower than the others.

Both Fujishiro's and Choy's results show an monotonic increase of thermal conductivity with temperature for Zylon, Dyneema bundles,¹² and Spectra 1000/low-density PE mixtures.¹¹ The steady-state heat flow method used by both research groups is subject to errors caused by radiation loss—especially for high aspect ratio samples at high temperature.⁴¹ Radiation errors were mentioned in ref 11 for measurements above 200 K of the composite consisting of Spectra 1000 and low-density PE.

Radiation errors in the conventional steady-state measurement are typically difficult, if not impossible, to estimate because the dominant source of error is typically radiation from the heaters and thermometers, not from the sample. The radiation error would be less important for nanofiber measurements due to the small length scales involved.⁴¹ For the PE nanofiber with a length of ~ 300 μm and a diameter of ~ 130 nm, the radiation loss derived following the method in ref 41 is less than 1%, which agrees with the analysis in the Supporting Information of ref 2.

While ref 12 does not discuss radiation errors, we note some apparent inconsistencies in the data: (i) extrapolation of the axial thermal conductivity of the fiber reinforced plastic with a volumetric filling factor of 0.6, and the thermal conductivity of embedding epoxy, predicts an $\Lambda \approx 33$ $\text{W m}^{-1} \text{K}^{-1}$ for both Zylon AS and Dyneema at 260 K, which is much smaller than those directly measured values for fiber bundles (≈ 60 $\text{W m}^{-1} \text{K}^{-1}$ for Zylon and ≈ 55 $\text{W m}^{-1} \text{K}^{-1}$ for Dyneema); (ii) conversion of the measured thermal diffusivities using 1.5 and 1.8 $\text{J cm}^{-3} \text{K}^{-1}$ as the volumetric heat capacities for Zylon and Dyneema at room temperature, gives $\Lambda \approx 16$ $\text{W m}^{-1} \text{K}^{-1}$ for Zylon and $\Lambda \approx 36$ $\text{W m}^{-1} \text{K}^{-1}$ for Dyneema, respectively, significantly smaller than the directly measured values.

We can gain insight into the order of magnitude for the phonon mean-free paths starting from the gas-kinetic equation in the Debye approximation, where Λ is calculated by integrating over phonon modes of frequency ω

$$\Lambda = \langle v_z^2 \rangle \int C(\omega) \tau(\omega) d\omega \quad (2)$$

where $C(\omega)$ and $\tau(\omega)$ are the volumetric heat capacity and the relaxation time of phonons at each frequency, and $\langle v_z^2 \rangle$ is the orientationally averaged z -component of the square of the sound velocity. The shear modulus ranges from 1 to 6 GPa for the fibers studied in this work,^{42,43} much smaller than the tensile modulus; therefore, we can expect that longitudinal modes are more important than shear modes in heat transport. Furthermore, because of the high degree of anisotropy, $\langle v_z^2 \rangle \approx v_l^2$.⁴⁴ In an isotropic material, the orientational averaging reduces the average velocity in the z -direction by a factor of 1/3; the importance of this phonon-focusing effect for anisotropic polymers has previously been discussed by Pietralla.^{45,46}

To obtain an order-of-magnitude estimate of the phonon mean-free path, we examine the relaxation time approximation, where τ is independent of frequency and describes the relaxation time of the longitudinal phonons that are most

important for heat transport. We estimate the heat capacity C of these vibrational modes as the product of the gas constant and the molar density. This estimate gives $C \sim 0.3$ $\text{J cm}^{-3} \text{K}^{-1}$ for polyethylene and $C \sim 0.06$ $\text{J cm}^{-3} \text{K}^{-1}$ for PBO. For a thermal conductivity of 20 $\text{W m}^{-1} \text{K}^{-1}$ and $v_l = 10$ km s^{-1} , we find $\tau \sim 0.7$ ps and $l = v_l \tau \approx 7$ nm for polyethylene and $\tau \sim 3$ ps and $l = v_l \tau \approx 30$ nm for PBO. The $1/T$ temperature dependence of the thermal conductivity suggests that the mean-free path l is limited by anharmonic decay of the longitudinal modes.

The relaxation time approximation is, of course, not an accurate description of phonon lifetimes. Since we have restricted the heat capacity in the calculation above to the longitudinal phonon modes, we believe that our estimates of $l \approx 7$ nm and $l \approx 30$ nm for polyethylene and PBO are approximately in the middle of the distribution of the mean-free paths of the longitudinal phonons; we point out, however, that the distribution of mean-free paths likely spans a wide range. For example, in Si, a similar analysis gives a dominant mean-free path of 300 nm at room temperature while the range of mean-free paths that are important in heat transport span 2 orders of magnitude, from 30 nm to 3 μm .⁴⁷

5. CONCLUSIONS

In summary, among the high modulus fibers that we examined, liquid crystalline PBO fibers have the highest room temperature thermal conductivity, $\Lambda \approx 20$ $\text{W m}^{-1} \text{K}^{-1}$, surpassing the conductivity of highly crystalline polyethylene. For both PBO and polyethylene, Λ near room temperature scales with temperature as $\Lambda(T) \propto 1/T$ consistent with Λ dominated by acoustic vibrational modes with coherence length or mean-free path limited by anharmonic decay. We estimate an average mean free path of ≈ 30 nm at room temperature for the longitudinal acoustic modes that are most likely to dominate the thermal transport in PBO. Higher thermal conductivities might be possible if the molecular structure or polymer morphology can be modified to increase the lifetimes of the high-frequency longitudinal acoustic modes that propagate along the rigid polymer chain.

■ ASSOCIATED CONTENT

Supporting Information

Details on the estimate of the temperature rise due to steady-state heating, uncertainty analysis about the model fitting, and 2D diffraction pattern from WAXS for fibers other than Dyneema and Zylon HM. This material is available free of charge via the Internet at <http://pubs.acs.org>.

■ AUTHOR INFORMATION

Corresponding Author

*E-mail: xwang58@illinois.edu (X.W.); d-cahill@illinois.edu (D.G.C.).

Notes

The authors declare no competing financial interest.

■ ACKNOWLEDGMENTS

This work is supported by AFOSR MURI FA9550-12-1-0002. We thank Prof. Economy and Mr. Meyer of UIUC for providing the Kevlar and Vectra samples and Prof. Gillespie and Dr. Leal at University of Delaware for providing the M5 AS samples. We are grateful to Honeywell, DSM LLC, TOYOBO Co., and AFRL for supplying the Spectra, Dyneema, Zylon, and

PBT samples, respectively. Sample characterization used facilities of the Center of Microanalysis of Materials and the Laser Facility of the Frederick Seitz Materials Research Laboratory (MRL) at UIUC and beamline 7.3.3 of the ALS at Lawrence Berkeley National Lab.

REFERENCES

- (1) Choy, C. L. *Polymer* **1977**, *18*, 984–1004.
- (2) Shen, S.; Henry, A.; Tong, J.; Zheng, R.; Chen, G. *Nat. Nanotechnol.* **2010**, *5*, 251–255.
- (3) Huang, X.; Liu, G.; Wang, X. *Adv. Mater.* **2012**, *24*, 1482–1486.
- (4) Choy, C. L.; Chen, F. C.; Luk, W. H. *J. Polym. Sci., Polym. Lett. Ed.* **1980**, *18*, 1187–1207.
- (5) Choy, C. L.; Luk, W. H.; Chen, F. C. *Polymer* **1978**, *19*, 155–162.
- (6) Hansen, D.; Bernier, G. A. *Polym. Eng. Sci.* **1972**, *12*, 204–208.
- (7) Choy, C. L.; Wong, Y. W.; Yang, G. W.; Kanamoto, T. *J. Polym. Sci., Part B: Polym. Phys.* **1999**, *37*, 3359–3367.
- (8) Washo, B. D.; Hansen, D. *J. Appl. Phys.* **1969**, *40*, 2423–2427.
- (9) Gupta, S.; Schieber, J. D.; Venerus, D. C. *J. Rheol.* **2013**, *57*, 427–439.
- (10) Mergenthaler, D. B.; Pietralla, M.; Roy, S.; Kilian, H. G. *Macromolecules* **1992**, *25*, 3500–3502.
- (11) Choy, C. L.; Fei, Y.; Xi, T. G. *J. Polym. Sci., Part B: Polym. Phys.* **1993**, *31*, 365–370.
- (12) Fujishiro, H.; Ikebe, M.; Kashima, T.; Yamanaka, A. *Jpn. J. Appl. Phys.* **1997**, *36*, 5633–5637.
- (13) Zheng, X.; Cahill, D. G.; Krasnochtchekov, P.; Averbach, R. S.; Zhao, J. C. *Acta Mater.* **2007**, *55*, 5177–5185.
- (14) Leal, A. A.; Deitzel, J. M.; Gillespie, J. W. *J. Compos. Mater.* **2009**, *43*, 661–674.
- (15) Thomsen, C.; Grahn, H. T.; Maris, H. J.; Tauc, J. *Phys. Rev. B* **1986**, *34*, 4129–4138.
- (16) Lapujoulade, J. *Surf. Sci. Rep.* **1994**, *20*, 195–249.
- (17) Vanormelingen, K.; Degroote, B.; Vantomme, A. *J. Vac. Sci. Technol., B* **2006**, *24*, 725–729.
- (18) Kang, K.; Koh, Y. K.; Chiritescu, C.; Zheng, X.; Cahill, D. G. *Rev. Sci. Instrum.* **2008**, *79*, 114901.
- (19) Ilavsky, J. *J. Appl. Crystallogr.* **2012**, *45*, 324–328.
- (20) Lyoo, H.-K.; Cahill, D. G. *Phys. Rev. B* **2006**, *73*, 144301.
- (21) Sperling, L. H. *Introduction to Physical Polymer Science*, 4th ed.; John Wiley & Sons, Inc: Hoboken, NJ, 2006.
- (22) Cahill, D. G. *Rev. Sci. Instrum.* **2004**, *75*, 5119–5122.
- (23) Koh, Y. K.; Cahill, D. G. *Phys. Rev. B* **2007**, *76*, 075207.
- (24) Yang, H.-S.; Cahill, D. G.; Liu, X.; Feldman, J. L.; Crandall, R. S.; Sperling, B. A.; Abelson, J. R. *Phys. Rev. B* **2010**, *81*, 104203.
- (25) Pernot, G.; Michel, H.; Vermeersch, B.; Burke, P.; Lu, H.; Rampnoux, J.-M.; Dilhaire, S.; Ezzahri, Y.; Gossard, A.; Shakouri, A. *MRS Proc.*, San Francisco, CA, 2011.
- (26) Minnich, A. J.; Johnson, J. A.; Schmidt, A. J.; Esfarjani, K.; Dresselhaus, M. S.; Nelson, K. A.; Chen, G. *Phys. Rev. Lett.* **2011**, *107*, 095901.
- (27) Eesley, G. L.; Clemens, B. M.; Paddock, C. A. *Appl. Phys. Lett.* **1987**, *50*, 717–719.
- (28) Graff, K. F. *Wave Motion in Elastic Solids*; Ohio State University Press: Columbus, OH, 1975.
- (29) Cahill, D. G.; Watanabe, F. *Phys. Rev. B* **2004**, *70*, 235322.
- (30) DSM Dyneema SK75 high-strength, high-modulus polyethylene fiber, Product Information Sheet.
- (31) Honeywell Spectra Fiber 900 High-Strength, Light-Weight Polyethylene Fiber, Product Information Sheet.
- (32) Honeywell Spectra Fiber 2000 High-Strength, Light-Weight Polyethylene Fiber, Product Information Sheet.
- (33) Vectra, Vectran Engineering Data.
- (34) Zylon Technical Information, TOYOBO Datasheet.
- (35) Kevlar149, <http://www.matweb.com>.
- (36) Gibson, A. G.; Greig, D.; Sahota, M.; Ward, I. M.; Choy, C. L. *J. Polym. Sci., Polym. Lett. Ed.* **1977**, *15*, 183–192.
- (37) Kim, Y. C.; Economy, J. *Polym. Adv. Technol.* **1999**, *10*, 493–500.
- (38) Caminiti, R.; Pandolfi, L.; Ballirano, P. *J. Macromol. Sci., Part B* **2000**, *39*, 481–492.
- (39) Fratini, A. V.; Lenhart, P. G.; Resch, T. J.; Adams, W. W. *MRS Proc.*, Boston, MA, 1988.
- (40) Northolt, M. G. *Eur. Polym. J.* **1974**, *10*, 799–804.
- (41) Cahill, D. G.; Pohl, R. O. *Phys. Rev. B* **1987**, *35*, 4067–4073.
- (42) *High-Performance Fibres*; CRC Press LLC: Boca Raton, FL, 2001.
- (43) Sikkema, D. J.; Northolt, M. G.; Pourdeyhi, B. *MRS Bull.* **2003**, *28*, 579–584.
- (44) Hsieh, W.-P.; Chen, B.; Li, J.; Keblinski, P.; Cahill, D. G. *Phys. Rev. B* **2009**, *80*, 180302.
- (45) Pietralla, M. *J. Comput.-Aided Mater.* **1996**, *3*, 273–280.
- (46) Pietralla, M.; Weeger, R. M.; Mergenthaler, D. B. *Z. Phys. B: Condens. Matter* **1989**, *77*, 219–228.
- (47) Yang, F.; Dames, C. *Phys. Rev. B* **2013**, *87*, 035437.